**Rare Metal Materials and Engineering**
Volume 49, Issue 8, August 2020
Available online at www.rmme.ac.cn

Science Press

**Cite this article as:** Rare Metal Materials and Engineering, 2020, 49(8): 2574-2582.

ARTICLE

# Microstructure and Wear Properties of Ni-based Composite Coatings on Aluminum Alloy Prepared by Laser Cladding

**Wu Xiaoquan**[1,2,3], **Yan Hong**[1,2], **Xin Yong**[1], **Yu Baobiao**[1,2], **Hu Zhi**[1], **Sun Yonghui**[1,2]

*[1] Nanchang University, Nanchang 330031, China; [2] Key Laboratory of Light Alloy Preparation & Processing in Nanchang City, Nanchang 330031, China; [3] Jiangxi University of Technology, Nanchang 330098, China*

**Abstract:** The microstructure and wear properties of Ni-based composite coatings on aluminum alloy prepared by laser cladding were investigated by SEM, EDS, microhardness tester and friction tester. The results show that there are relatively few holes and cracks in the layer when the scanning speed is 5 mm/s. Many massive and continuous network Ni-Al intermetallic compounds form on the top of the cladding layer, and (Ni, Cr, Fe)$_x$C$_y$ intermetallic compounds form at the middle of the cladding layer. The microstructure of the bottom cladding layer consists of the columnar $\alpha$-Al dendrite with obvious growth direction. The middle and top of the cladding layer maintain a high microhardness value. The maximum microhardness of the middle of layer is 8200 MPa, which is more than 5 times larger than that of the bottom cladding layer. The microhardness decreases sharply at the end of the middle of layer. The friction coefficients of the layer have a fluctuation under different loads, and decrease with increasing the load. The formation and distribution of Ni-Al and (Ni, Cr, Fe)$_x$C$_y$ intermetallic on the top and middle of the cladding layer are the primary reason for the improvement of the microhardness and wear of the layer.

**Key words:** laser cladding; aluminum alloy; Ni-base composite; Ni-Al intermetallic compounds; (Ni, Cr, Fe)$_x$C$_y$ intermetallic compounds

Aluminum alloy is widely used in aerospace and automobile manufacturing because of its low density and high specific strength[1,2]. However, aluminum alloy is limited in industrial applications because of its poor toughness, low hardness, and poor corrosion resistance. Laser cladding on the surface of aluminum alloy is one of the most effective methods to solve these problems[3-5]. Laser cladding is clean, efficient and has a high bonding strength compared with others[6,7]. Variety of non-equilibrium solids can be formed in the layers under the conditions of temperature gradient and supercooling. The cladding layer exhibits high microhardness, wear resistance and corrosion resistance[8,9]. Therefore, the technology of laser cladding has a very broad application prospects in the surface treatment of metal materials.

For laser cladding technology, the design of the cladding alloy powder and the choice of reinforcement material are vital[10-12]. Cladding powders are required to be the same as the matrix or self-fluxing powders due to the selection principles of thermal expansion and the melting point of the cladding materials. Self-fluxing powders, such as Ni-based, Co-based, and Fe-based mixing powder, are more common in the market. Xu et al[13] successfully fabricated Ti-Al-Fe-B coatings via laser cladding on the surface of 7075 aluminum alloy. It is found that when the content of TiBCN is 15%, the microhardness of the cladding layer is 7500 MPa, which is 5 times higher than that of the substrate. Additionally, the corrosion current is also lower than that of the substrate. The wear tests show that the mass loss of the cladding layer is only 2.4 mg in 20 min, which is much lower than that of the matrix. Wang et al[14] prepared the Ni+La$_2$O$_3$, Y$_2$O$_3$, and CeO$_2$ layer on the surface of 6063Al. The resulting cladding layer is composed of $\beta$-NiAl (Cr), Al$_3$Ni, AlNi$_3$, and Al phases. Additionally, the microhardness successively decreases from the top to the bottom of the cladding layer.

Ni alloys are often used as matrix materials for cladding powders because of their good corrosion resistance, low

---

Received date: August 13, 2019
Foundation item: Natural Science Foundation of Jiangxi Province, China (20181BAB206026, 20171BAB206034)

Corresponding author: Yan Hong, School of Mechanical and Electrical Engineering, Nanchang University, Nanchang 330031, P. R. China, Tel: 0086-791-83969633, E-mail: hyan@ncu.edu.cn

thermal expansion and easy metallurgical bonding with the matrix[15]. The elements B and Si are often added to Ni-based powder because they can effectively reduce cracks, holes, and other defects in the cladding layer[16].

70% of the automotive aluminum alloy parts are casted; however, the hardness, wear resistance, and other mechanical properties of Al-Si alloys are far lower than those of steel [17]. Under the harsh working conditions of automotive engines, such as high temperature, high pressure, and difficulty of lubrication, aluminum alloy parts are prone to wear, corrosion, and other failures[18]. The AlSi7Mg alloy has excellent mechanical properties at room and high temperatures, and it is often used to manufacture pistons for automotive engines.

In this research, Ni-based composite powder was used as cladding material to modify the surface of an AlSi7Mg alloy via the synchronous-powder-feeding method and to improve the surface properties of the alloy.

## 1 Experiment

### 1.1 Experimental equipment

Nd:YAG solid-state laser (JHL-1GX-2000 laser processing machine) was used in experiment with a wavelength of 1064 nm, which is produced by the Chutian Company in Wuhan. The laser cladding material was prepared by synchronous feeding. The diagrammatic sketch of laser and the specific processing parameters are shown in Fig.1 and Table 1, respectively. The microstructures of the samples were examined via optical microscopy (OM, Nikon, MA-200) and scanning electron microscopy (SEM, QUANTA-200). The polished sample was tested for microhardness by Vivtorinox (HXS-1000A). The cross-section of the layer was detected from the surface to the bottom at 100 μm intervals under 0.1 kg preloading and 15 s preloading time conditions.

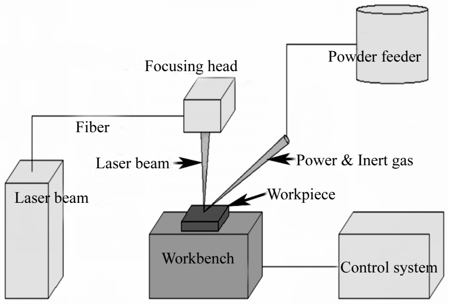

Fig.1 Scheme of laser cladding station

**Table 1 Laser processing parameters**

| Sample | Laser output power/W | Scanning velocity/mm·s$^{-1}$ | Laser beam size/mm | Shielding gas flow rate/ L·min$^{-1}$ |
|---|---|---|---|---|
| 1 | 1200 | 3 | 1.2 | 2.5 |
| 2 | 1200 | 5 | 1.2 | 2.5 |
| 3 | 1200 | 8 | 1.2 | 2.5 |

In the wear experiment, corundum with Mons' scale of hardness 9 was selected as friction coupling. Its size was *Φ*40 mm×10 mm. The diagrammatic sketch of wear device and the processing parameters are show in Fig.2 and Table 2, respectively. The wear samples were processed into cylindrical samples with a diameter of 4.5 mm and a height of 10 mm by wire-electrode cutting. The samples polished with 1000# and 2000# sandpaper and friction coupling were soaked in absolute ethanol, and then cleaned by ultrasonic waves.

### 1.2 Experimental materials

The composition of the AlSi7Mg alloy in the laser cladding process is shown in Table 3. The samples were directly cut from ingot and processed into 100 mm×50 mm×12 mm plates. After being sanded by 400# sandpaper, the surface oxide layer was cleaned with ethanol and dried.

The melting point of the Ni based self-fluxing composite powder shown in Fig.3 is 960~1040 °C [19]. The ingredients of 150~325 mesh powders after drying at 100 °C for 2 h were used in the experiment, as shown in Table 4.

## 2 Results

### 2.1 Macromorphology of layer at different scanning speed

The macromorphologies of cross section of the AlSi7Mg cladding layer obtained at different scanning speeds are shown in Fig.4. The layer can be divided into zones A, B, C and D according to the difference of temperature gradient, which are marked in Fig.4a. Zone A is the top area of the cladding layer, which is characterized by high supercooling. Zone A is called the fine-grained region due to homogeneous composition and

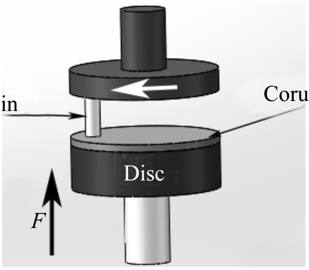

Fig.2 Diagrammatic sketch of wear device

**Table 2 Processing parameter of wear experiment**

| Sample | Rotating speed/r·min$^{-1}$ | Load/N | Time/s |
|---|---|---|---|
| 1 | 100 | 20 | 900 |
| 2 | 100 | 40 | 900 |
| 3 | 100 | 60 | 900 |
| 4 | 100 | 80 | 900 |

**Table 3 Chemical composition of aluminum alloy substrate (wt%)**

| Si | Fe | Cu | Mg | Ti+RE | Mn | Zn | Al |
|---|---|---|---|---|---|---|---|
| 7.5 | 0.5 | 0.2 | 0.25 | 0.25 | <0.35 | <0.3 | Bal. |

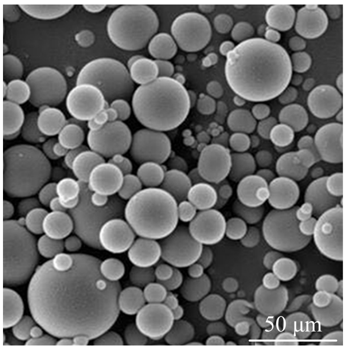

Fig.3 SEM image of Ni-base mixed powder

**Table 4 Chemical composition of Ni-base alloy powder (wt%)**

| Cr | Fe | Si | B | C | Ni |
|---|---|---|---|---|---|
| 18 | 8.0 | 4.0 | 3.2 | 0.6 | Bal. |

large temperature gradient. The characteristic of zone B is constitutional supercooling in the center of the melt, which is called the equiaxed dendritic region. Zone C includes transition zone and heat affected zone in the bottom of the melt. The dendrite growth has an obvious orientation in transition zone. Zone D is the substrate.

Referenced in Fig.4b~4d, the thicknesses of the melting zones of the layer are about 780, 850, and 790 μm, respectively. It is evident that there are cracks on the surface of the cladding layers at different scanning speeds, as shown in point 1 in Fig.4b. Cracks exist in alloy at 3 mm/s speed. However, when the speed increases to 5 mm/s (Fig.4c), fewer cracks appear in the layer. At the 8 mm/s speed (Fig.4d), the cracks are accompanied by many holes with 50 μm in size.

The cracks mainly appear at the top of the layer because there is a large temperature gradient on the surface of the cladding layer. It indicates that the thermal stress is the main cause of crack formation. The layer prepared at low scanning speed has longer local heating time and higher heat absorption than that prepared at high scanning speed. Therefore, cracks are more likely to be generated on the surface of layer at low speed. Fig.4b and 4c indicate that many cracks appear at the top of the cladding layer and fewer cracks appear in the middle of the layer. The reason for this discrepancy is that with the increase of the scanning speed, the heating time of the layer is reduced, so the heat absorption of the layer is decreased. Therefore, the thermal stress in the middle of the layer is weakened. As can be seen from Fig.4d, the pores and cracks in the layer with scanning speed of 8 mm/s are obviously larger than those in the layer with scanning speed of 5 mm/s. Additionally the thickness of the layer with scanning speed of 8 mm/s is less than that of the layer with scanning speed of 5 mm/s. The reasons for this difference are that with the increase of scanning speed, the crystallization of velocity accelerates, the solidification time of molten pool becomes faster, and the composite powders are less heated. Ultimately,

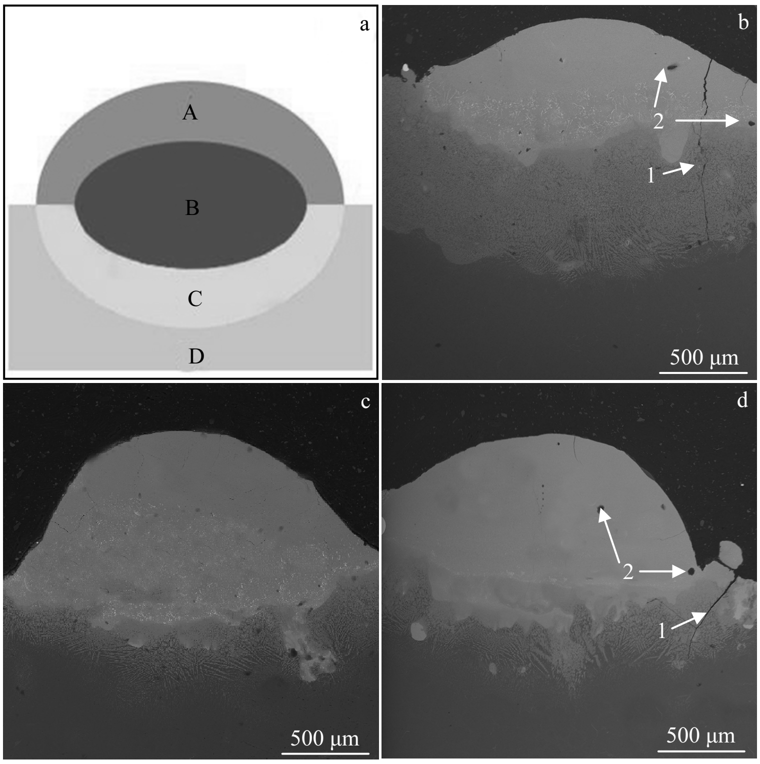

Fig.4 Macroscopic images of cladding layer at different speeds: (a) schematic diagram, (b) 3 mm/s, (c) 5 mm/s, and (d) 8 mm/s

the parts of particles cannot be fully melted or more likely to form holes. Additionally, some of the particles are blown away by the process of synchronous powder feeding. Therefore, the size of the layer at a high speed becomes thinner and the number of holes increases. In addition, the crystallization speed of the molten pool may also be improved with the increase of scanning speed. In the solidification and phase transition process, the increase of crystallization speed leads to the decrease of gas solubility. The residual protective gas $N_2$ and some $H_2$ and $H_2O$ gases produced during metallurgical reaction cannot be released timely, causing the formation of the holes in the alloy during solidification. Therefore, the holes in the cladding layer are eventually formed. In conclusion, the thickness of the layer increases first and then decreases with the increase of scanning speed and the porosity in the layer increases. The main cause of crack formation on the surface of the cladding layer is thermal stress.

### 2.2 Microstructure and composition of layer

Fig.5a is SEM image of the top of the layer, which is a boundary between zone A and B. The microstructure of the zone A which is composed of fine equiaxed grains is very homogeneous. A large number of dendrites can be seen in the zone B. Fig.5b is a SEM image of the bottom of the layer, which is a boundary between zones C and D. The bottom area of the melt consists of the transition zone and the heat affected zone. There are many columnar dendrites in the transition zone of layer. The growth direction of these columnar dendrites is from the matrix to the melt center.

Fig.6 is the SEM images and EDS results of the zones A, B and C which are shown in Fig.4. Fig.6a indicates that many equiaxed grains form at point 1 and continuous reticulate branches at point 2 around point 1. No obvious precipitates are found in the equiaxed grains and reticulate dendrites. According to the result of EDS, the main components of point 1 and point 2 are Ni, Al, Fe, and Si, but the contents of Ni and Si atoms differ greatly.

Fig.6b illustrates the SEM and EDS results of zone B, which has obvious branch structure besides equiaxed and reticulated dendrites. The results of EDS of the branches illustrate that the peaks of Ni, Al, Cr, Fe and C appear at point 3. Fig.6c illustrates the columnar morphology in zone C, which is mainly composed of Al.

According to the reaction between Ni and Al, the following chemical reactions may occur for the melt [20-23]:

$$3Ni+Al \rightarrow Ni_3Al \quad (1)$$

$$Ni+Al \rightarrow NiAl \quad (2)$$

$$2Ni+NiAl \rightarrow Ni_3Al \quad (3)$$

According to the thermodynamic conditions and the Gibbs free energy criterion [24-26]:

$$\Delta G=\sum G_p-\sum G_R \quad (4)$$

In the above formula, $G_p$ is the free energy of the product, and $G_R$ is the free energy of the reactant. The Gibbs free energy values of the above three reactions (Eq.(1~3)) at 1200 °C are −127.36, −96.51 and −30.85 kJ/mol, respectively[23]. The negative Gibbs free energy values indicate that all the reactions can be carried out thermodynamically.

Fig.6a illustrates that the atomic ratios of Ni and Al at point 1 and point 2 are 58:50 and 61:50, respectively. According to the chemical reactions between Ni and Al, it is inferred that the *β*-NiAl is precipitated directly from the liquid phase, and the Ni-rich and aluminum-poor liquid environment is then formed around the precipitated phase. The existence of Ni-rich areas creates condition for the formation of $Ni_3Al$. Yu et al[27] in-situ synthesized $Ni_3Al$ intermetallic compound phase coating by laser cladding using preplaced Ni and Al mixed powders. It is found that the laser power density and energy density have a crucial influence on the microstructure and tribological properties of the $Ni_3Al$ coating. In addition, they investigated the single phase NiAl coating by laser cladding at elevated temperature of 800 °C. It is found that $Ni_3Al$ phase with a fine equiaxial microstructure precipitates along NiAl grain boundaries via the solid-state diffusion of Ni atoms during heating process [28]. Therefore, according to the SEM and EDS results, it can be inferred that the massive and networked intermetallic compound in Fig.6a is NiAl and $Ni_3Al$ phases.

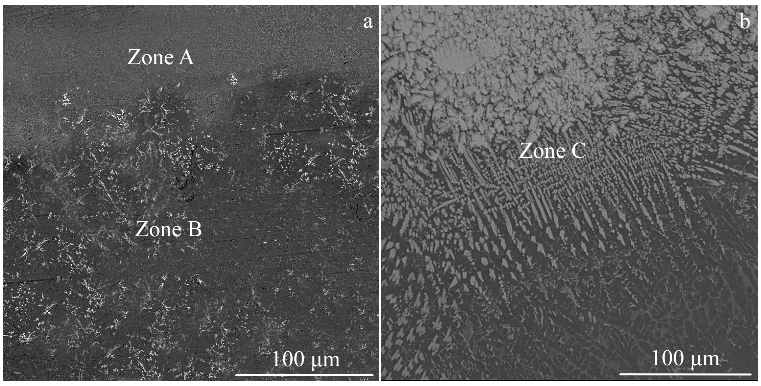

Fig.5 SEM images of the layer of the alloy at scanning speed of 5 mm/s: (a) zone A and B; (b) zone C

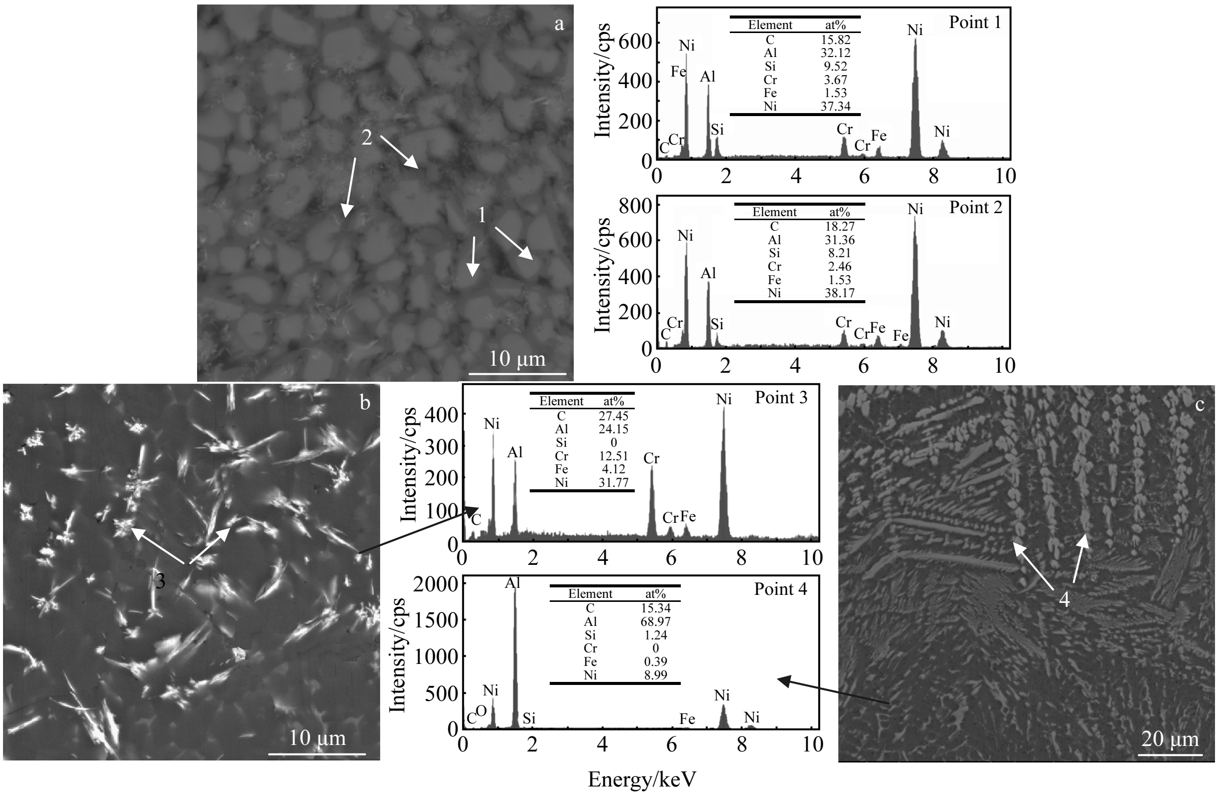

Fig.6 SEM images and EDS results of zone A (a), zone B (b), and zone C (c) in Fig.4

Fig.6b illustrates the microstructure of the middle of the layer, which is the frontier of columnar crystallization. According to the solidification theory of metals, melt has component supercooling in the middle of the layer. Meanwhile, there is melt convection in the molten pool in the middle of the layer. These factors have a comprehensive effect on the microstructure of zone B. When the melt temperature reaches above 1500 °C, the primary carbide $M_7C_3$ is first crystallized in the liquid phase. The specific equation for this is $L \rightarrow M_7C_3$[29]. With the further decrease in temperature, the following three kinds of eutectic transformations occur [29-32]:

$$L \rightarrow M_7C_3 + M_{23}C_6 \tag{5}$$

$$L \rightarrow \gamma(\mathrm{FeCr}) + M_7C_3 \tag{6}$$

$$L + M_{23}C_6 \rightarrow \gamma(\mathrm{FeCr}) + M_7C_3 \tag{7}$$

Zhang[33] coated the Ni-$Cr_3C_2$ and Ni-WC with overlapping clad tracks (OCT) on martensitic stainless steel. The coating is composed of $\gamma$-$M_7C_3$ eutectic and granular solidified structure. Tan[34] fabricated the $Al_2O_3$-$M_7C_3$ particle reinforced iron matrix composite coatings on a steel substrate by laser cladding using Fe-based alloy powder and Al/$Fe_2O_3$ thermite reactants. Chiang[35] deposited the stellite12 cobalt base alloys on SK3-carbon tool steel by laser cladding. The result show that the Co, $M_{23}C_6$, $M_6C$ and $M_7C_3$ ($M$ = W, Cr, Co) exist in the layer.

Under the experimental conditions, the solidification mode of the melt is the same as above, and the morphology of the formed phase is also the same. Therefore, according to the SEM and EDS results, it can be inferred that the intermetallic compound of point 3 in Fig.6b is $(Ni, Cr, Fe)_7C_3$ phase which is defined as $M_7C_3$.

Ni-Al is an exothermic reaction with high latent heat of melt crystallization, which creates conditions for $(Ni, Cr, Fe)_7C_3$ dendrite growth. The growth of the secondary dendrite is hindered under the convection of the melt. Secondary dendrites are interrupted by melt convection to form new nucleation, so they are small dendrites in zone B.

Fig.6c is a columnar grain in the zone C of the layer, which is non-spontaneous nucleation. Zone C is a transition zone and also a liquid-solid boundary zone. Owing to the low melting point of Al, a part of Al matrix is usually burned in laser cladding. However, the aluminum in the matrix is well-preserved. The main reason is that the protective gas is used in the cladding process. In addition, the addition of Cr and Fe into Ni-based cladding material reduces the melting point of cladding material. These two factors make the burning loss of Al less in the experiment.

Fig.7 is the composition distribution of the zones A~C of the layer. The distribution of the Ni content in the zone B decreases first and then increases, and it drops sharply in zone C. There is a high percentage of Al in the zone A, and it begins to decrease when entering zone B, and then increases rapidly in zone C. The atomic percentage of C, Cr, and Fe begins to increase in the zone B. The primary reasons are the large

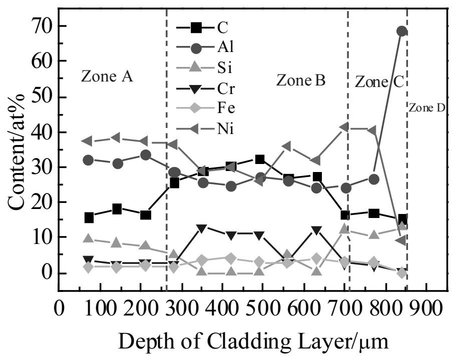

Fig.7 Component distribution of the cross section of layer at scanning speed of 5 mm/s

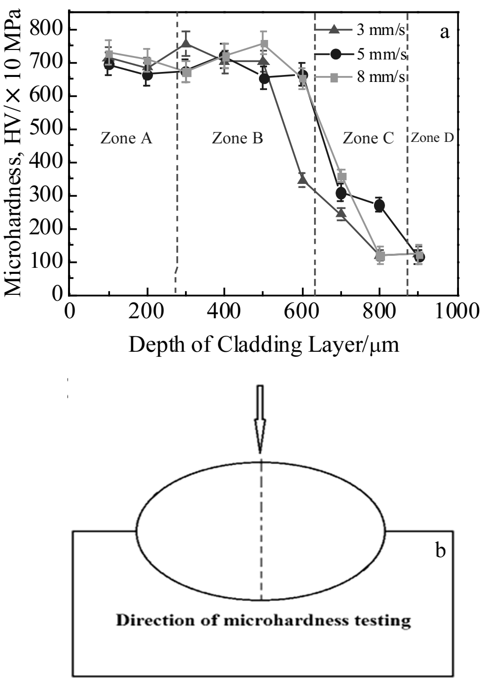

Fig.8 Microhardness of the cladding layer along the cross section at different scanning speeds (a) and diagrammatic sketch of direction of microhardness testing (b)

supercooling, fast crystallization speed and high temperature gradient in zone A, which refine the grain and make the composition uniform. Therefore, the content of elements in zone A fluctuates little.

Due to the small supercooling and temperature gradient in zone B, the content of C and Cr increases obviously. Therefore, the grains in the zone B grow upward. The content of other elements decreases rapidly except for the rapid increase of Al content in the zone C near the matrix.

## 3 Microhardness and Wear Properties Analyses

Fig.8a is the microhardness curves of the cladding layer along the cross section at different scanning speeds. Fig.8b is schematic of microhardness testing. The micro- hardness of zone D is about 1300 MPa and the microhardness of zone C ranges from 1800 MPa to 3000 MPa, which is 1.5 times larger than that of the matrix. The microhardness of zone B is in the range of 6200~8200 MPa, and that of zone A is about 7300 MPa. It is found that the coating is thin and the microhardness of the coating decreases at 510 μm depth when the scanning speed is 3 mm/s. The maximum microhardness of all samples appears in the zone B of the layer, which is more than 5 times larger than that of the bottom of the cladding layer. The main reason is that the reinforcing phases of NiAl and $M_7C_3$ are formed in the zone B, and their microhardness is 7000 and 9000 MPa, respectively[31]. Additionally, the NiAl content decreases at the junction of zones B and C, resulting in a decrease in microhardness. The microhardness of zone A is about 7000 MPa. The microhardness near the coating surface is higher than at the bottom of the coating because fine equiaxial crystals form on the surface of the coating and coarse columnar crystals form at the bottom of the coating. In addition, the formation of NiAl and $Ni_3Al$ phases on the top of the coating leads to obvious improvement in microhardness of the zone A.

As shown in Fig.9a, with scanning speed of 5 mm/s for 15 min under loads of 20, 40, 60, and 80 N, the average friction coefficient of cladding layer is obtained by mean value of instantaneous friction coefficient. It illustrates that the average friction coefficients of the layers range from 0.37 to 0.43, and decrease with increasing the loads. Fig.9b~9e illustrate the instantaneous friction coefficient under loads of 20, 40, 60, and 80 N for 15 min. As shown in Fig.9b, with increasing the time, the fluctuation of instantaneous friction coefficient shows a great change when the loading is 20 N. This is because the materials move relative to the friction coupling, and the contact surfaces consist of very small contacts rather than face-contact. The fluctuation of friction coefficients has little change under the loading of 40 and 60 N. The instantaneous friction coefficient of the coating increases when the friction time is 250 s, and then decreases continuously under the loading of 80 N. This is because the gradient of the microhardness of the layer leads to the gradient change of the friction coefficient.

Fig.10 is SEM images of the friction surface of layer under different applied loads. As shown in Fig.10, the friction surfaces of the specimen have a plough-shaped appearance. When the load is less than 60 N, the width of the wear scratches increases with the increase of loading. When the load is 80 N, the wear scratches are no longer widened and the plastic deformation zone appears on the frictional surface. The friction surface of layer exhibits a slight scratch under the loading of 20 N. Under the 40 N loading, there are smooth scratches on the friction surface of layer, which are wider than that under 20 N loading. The friction surface shows wider scratches and some areas exhibit plastic deformation under the

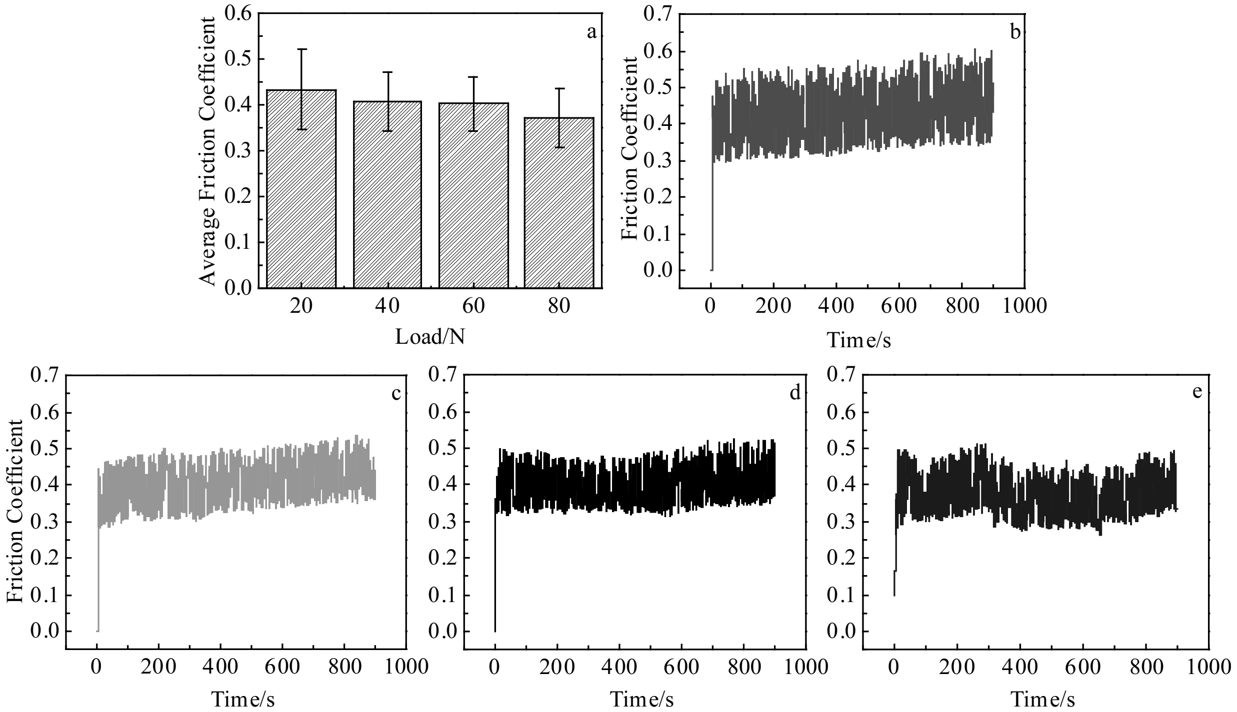

Fig.9 Average friction coefficient of cladding layer with scanning speed of 5 mm/s for 15 min under different loads (a); instantaneous friction coefficient of cladding layer under 20 N (b), 40 N (c), 60 N (d), and 80 N (e)

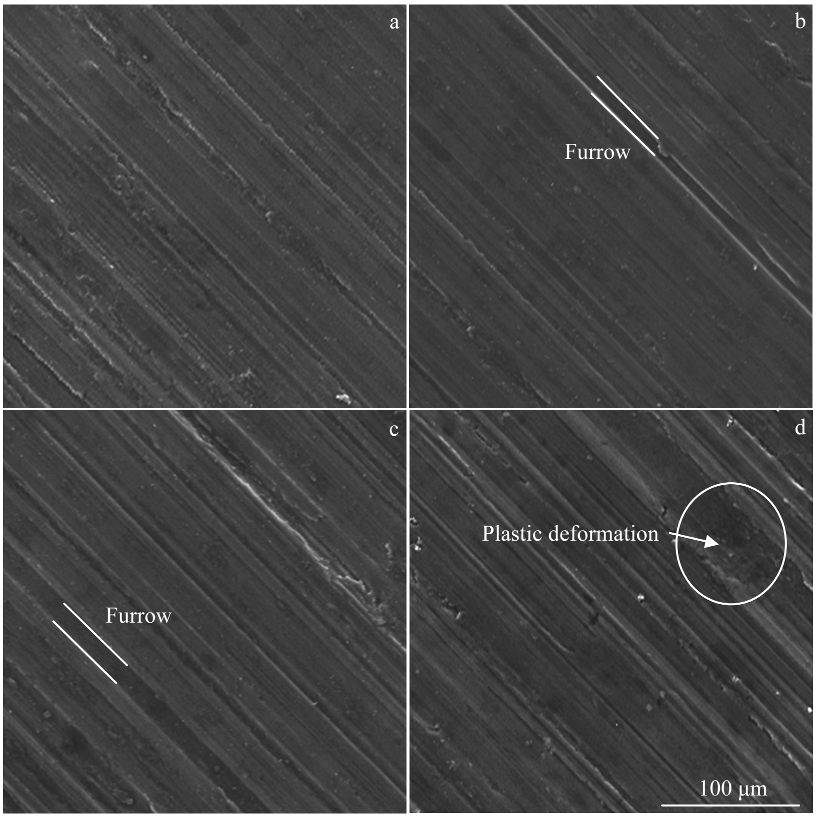

Fig.10 SEM images of friction surface of layer under different loads for 15 min: (a) 20 N, (b) 40 N, (c) 60 N, and (d) 80 N

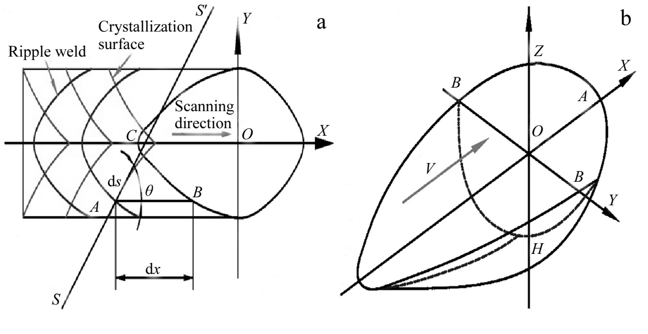

Fig.11 Relationship between grain growth, scanning speed and crystallization surface (a) and molten pool model (b)

60 N loading. Some particulates are distributed on the friction surface and lip appears on the two sides of plough under the 80 N loading. It means that the friction surface plastic deformation occurs. This is because increase of loading causes the plastic deformation and debris causes the scratches on the sample.

## 4 Discussion

During crystallization, the direction of grain growth in the molten pool is closely related to the linear growth speed of primary dendrite and the laser scanning speed [36].

Fig.11 illustrates the relationship between grain growth and scanning speed and the molten pool. The growth direction of the core of any grain at any point in A is the tangent direction of this point on *A* (*S*-*S′* line), as shown in Fig.11a. The angle between this direction and *X* axis is *θ*. If the crystallization isothermal surface moves along the *X*-axis in d*t* time, the crystallization surface moves from *A* to *B*, and the grain growth direction is from *A* to *C*. Δ*ABC* can be regarded as a right triangle when the value of d*x* is very small, and then the $ds=dx\cos\theta$ can be obtained. By dividing d*t* from both sides of the equation, the relationship between the average of the linear velocity of grain growth and the laser scanning speed can be obtained as follows[37-39]:

$$V_c=V\cos\theta \quad (8)$$

In the above equation, $V_c$ is the average linear velocity of grain growth, *V* is the laser scanning speed, and *θ* is the angle between the $V_c$ and *V* direction.

In the *A* zone, the grain growth rate of the melt surface is the highest, the linear velocity of the grain growth is equal to the scanning speed ($\theta$=0, $V_c=V$), and zone A has a large heat exchange coefficient since it directly in contact with air. Therefore, the melt of zone A has a large supercooling and temperature gradient (Fig.11b). The above factors provide the conditions for grain nucleation and grain refinement. Therefore, the microstructure of zone A is fine equiaxed grain. In the molten pool with small temperature gradient and constitutional supercooling, the growth of dendrites has favorable conditions in zone B. Convection in melt is the main factor affecting grain growth. However, due to the convection in the melt center, it is easy to break the dendrites and form a new crystal nucleus in the convection process, which leads to the underdevelopment of many secondary dendrites. Many dendrites are distributed evenly in the zone B.

In the zone C, the linear velocity of grain growth is zero for $\theta$=90° and $V_c$=0. In laser cladding, the grain of the matrix surface is heated, and the non-spontaneous nucleation of the melt is attached to the solid-liquid interface. Additionally, the zone C has small convective intensity and a large temperature gradient, which provide favorable conditions for columnar crystal growth. The primary dendrites of columnar dendrites are developed and have an obvious directivity. Therefore, Fig.5b shows a large number of directional columnar crystals.

## 5 Conclusions

The Ni-based self-fluxing coating is successfully prepared by laser cladding technology on the surface of AlSi7Mg. The microstructure and the wear properties of the cladding layer are analyzed and discussed.

1) A Ni-based self-fluxing coating cladding layer without pores and with a few cracks is prepared on the surface of AlSi7Mg alloy at a scanning speed of 5 mm/s.

2) The top of layer is composed of fine NiAl equiaxed crystals and continuous network structure of $Ni_3Al$. The middle part of the layer consists of the compounds of Al, Ni, C, Fe, and Cr. The bottom of the layer is a mixed zone consisting of transition zone and heat-affected zone, in which a quantity of columnar crystals form. The growth direction of columnar crystals is perpendicular to the melt interface and points to the melt center. The mechanism of directional columnar crystals is revealed according to the relationship between laser scanning speed and grain growth.

3) The middle and the top of the cladding layer maintain a high microhardness value. The microhardness of the middle cladding layer has a maximum value of 8200 MPa, which is more than 5 times larger than that of the bottom of the cladding layer. The microhardness decreases sharply in the end of the middle of the layer.

4) The friction coefficient of the layer decreases with increasing the load, and the average friction coefficients of the layer range from 0.37 to 4.3. The instantaneous friction coefficient of the layer increases when the friction time is 250 s, and then decreases continuously under a loading of 80 N.

## References

1 Kwok C T, Man H C, Cheng F T *et al. Surface and Coatings Technology*[J], 2016, 291: 189

2 Singh I B, Mandal D P, Singh M *et al. Corrosion Science*[J], 2009, 51: 234

3 Zhao H, De G F, Silva A K D. *Acta Materialia*[J], 2018, 156: 318

4 Wu Qingjie, Yan Hong, Liu Yuan. *Rare Metal Materials and Engineering*[J], 2018, 47(3): 742

5 Puga H, Barbosa J, Costa S. *Materials Science and Engineering*

*A*[J], 2013, 560: 589

6 Song M S, Zhang M X, Zhang S G *et al. Materials Science & Engineering A*[J], 2018, 473: 166

7 Babu K T, Kumar P K, Muthukumaran S P. *Procedia Materials Science*[J], 2014, 6: 648

8 Yang Y, Wu H. *Materials Letters*[J], 2009, 63(1): 19

9 Lijay K J, Selvam R J, Dinaharan I *et al. Transactions of Nonferrous Metals Society of China*[J], 2016, 26(7): 1791

10 Yan Y, Pan C L, Zhang R H. *Journal of Alloys & Compounds*[J], 2018, 765: 782

11 Wang C L, Gao Y G, Wang R. *Journal of Alloys & Compounds*[J], 2018, 740: 1099

12 Cai X, Yang X Y, Chen Q L *et al. Journal of Materials Engineering*[J], 2000, 4: 6

13 Xu J, Liu W, Kan Y. *Materials & Design*[J], 2006, 27(5): 405

14 Wang C L, Gao Y, Zeng Z C *et al. Journal of Alloys & Compounds*[J], 2017, 727: 278

15 Shu D, Li Z G, Zhang K. *Materials Letters*[J], 2017, 195: 178

16 Lei Jianbo, Shi Chuan, Zhou Shengfeng *et al. Surface & Coatings Technology*[J], 2018, 334: 274

17 Zhang Xiaolin, Zhang Kemin, Ma Jinxin *et al. Journal of Minerals and Materials Characterization and Engineering*[J], 2017, 5: 29

18 Basavakumar K G, Mukunda P G, Chakraborty M. *Materials Characterization*[J], 2008, 59(3): 283

19 Wang X Y, Zhou S, Dai X *et al. International Journal of Refractory Metals & Hard Materials*[J], 2017, 64: 234

20 Volovitch P, Masse J E, Fabre A *et al. Surface & Coatings Technology*[J], 2008, 202(20): 4901

21 Tsao C L, Chen S W. *Journal of Materials Science*[J], 1995, 30: 5215

22 Kecskes L J, Szewczyk S T, Peikrishvili A B. *Metallurgical and Materials Transactions A*[J], 2004, 35: 1125

23 Anita O M. *Microchimica Acta*[J], 2004, 145: 133

24 Cui H Z, Wei N, Zeng L L. *Transactions of Nonferrous Metals Society of China*[J], 2013, 23(6): 1639

25 Li H P. *Journal of Materials Science*[J], 2008, 43(5): 1688

26 Salje E K H, Zhang H, Schryvers D. *Applied Physics Letters*[J], 2007, 90(22): 159

27 Yu Y J, Zhou J S, Chen J M *et al. Intermetallics*[J], 2010, 18(5): 871

28 Yu Y J, Zhou J S, Yang L B *et al. Rare Metal Materials and Engineering*[J], 2012, 41(1): 116

29 Mayer S, Leitner H, Scheu C. *Steel Research International*[J], 2010, 80(1): 89

30 Samuels L E, Mann S D. *Materials Characterization*[J], 1997, 38(4-5): 233

31 Lee B J Y. *Metallurgical Transactions A*[J], 1993, 24(5): 1017

32 Lemkey F D, Gupta H, Nowotny H. *Journal of Materials Science*[J], 1984, 19(3): 965

33 Zhang Dawei, Zhang Xinping. *Surface & Coatings Technology* [J], 2005, 190(2-3): 212

34 Tan H, Luo Z, Li Y *et al. Wear*[J], 2015, 324-325: 36

35 Chiang K A, Chen Y C. *Journal of Materials Processing Technology*[J], 2007, 182(1-3): 297

36 Silva W S D, Souza R M, Mello J D B *et al. Wear*[J], 2011, 271(9-10): 1819

37 Liu X G, Guo H D, Yu M M. *International Journal of Computational Methods*[J], 2017, 16: 1 840 023

38 Shi Yaowu, Chen Dong, Lei Yongping. *Computational Materials Science*[J], 2004, 31(3-4): 385

39 Zhan X H, Dong Z B, Wei Y H. *Crystal Research & Technology* [J], 2009, 44(4): 414

# 铝合金表面激光熔覆镍基复合涂层的组织与磨损性能

吴孝泉[1,2,3]，闫　洪[1,2]，辛　勇[1]，喻保标[1,2]，胡　志[1]，孙勇辉[1,2]

(1. 南昌大学，江西 南昌 330031)

(2. 南昌市轻合金材料制备与加工重点实验室，江西 南昌 330031)

(3. 江西科技学院，江西 南昌 330098)

**摘　要**：利用 SEM、EDS、磨损试验机及硬度测试仪等设备对铝合金表面激光熔覆层的组织与磨损性能开展了研究。结果表明，当扫描速度为 5 mm/s 时，熔覆层气孔、裂纹等缺陷相对较少；在熔覆层顶部生成了许多块状及网状的 Ni-Al 金属间化合物，中部生成了$(\text{Ni, Cr, Fe})_x\text{C}_y$金属间化合物，底部存在大量具有明显生长方向性的柱状 $\alpha$-Al 枝晶。熔覆层顶部及中部保持着高硬度值，中部硬度最高值达 8200 MPa，是熔覆层底部硬度值的 5 倍以上。硬度值在熔覆层中部的末端开始显著下降。熔覆层的摩擦系数根据载荷不同其值在 0.37~0.43 间变化，并随着载荷增加而有所降低。Ni-Al 和$(\text{Ni, Cr, Fe})_x\text{C}_y$金属间化合物等强化相在熔覆层中的生成及其在在熔覆层中上层的均匀分布是改善材料硬度及磨损性能的主要原因。

**关键词**：激光熔覆；铝合金；镍基复合材；Ni-Al金属间化合物；$(\text{Ni, Cr, Fe})_x\text{C}_y$金属间化合物

---

作者简介：吴孝泉，男，1980 年生，博士，南昌大学机电工程学院，江西 南昌 330031，电话：0791-83969633，E-mail: wxq177@sina.com